



Effects of heat treatment on surface integrity and wear performance of Inconel 718 alloy fabricated by laser powder bed fusion process additive manufacturing under different laser power and scanning speed parameters

Nedim Sunay¹ · Mert Kaya² · Mustafa Safa Yılmaz³ · Yusuf Kaynak⁴

Received: 10 October 2022 / Accepted: 10 June 2023

© The Author(s), under exclusive licence to The Brazilian Society of Mechanical Sciences and Engineering 2023

Abstract

As with all additive manufacturing processes, selecting appropriate process parameters in the laser powder bed fusion (LPBF) process plays an important role in the surface integrity and mechanical behavior of Inconel 718 components. Hatch distance, laser power, laser scanning speed and layer thickness are the main parameters that can be altered in the LPBF process. This study focuses on the role of laser power and scanning speed when hatch distance is larger than laser spot size on product properties. This work reveals that LPBF process parameters significantly impact the fabricated Inconel 718 material properties. However, although the material properties are enhanced by selecting appropriate process parameters, the components need post-processing methods to have the desired properties. Heat treatment was applied as a post-process to obtain parts with the desired material properties. The effect of heat treatment applied to the parts fabricated at various laser power and laser scanning speeds on the parts' surface integrity, and mechanical performance is comprehensively presented. Determining the details of the interactions of different production parameters with heat treatment is one of the motivations of this study. The presented results establish that heat treatment can change specimens' microstructural aspects. The results also show a 10% increase in microhardness and a 14% increase in wear performance of specimens, due to the final state of the microstructure after heat treatment.

Keywords Additive manufacturing · Surface integrity · Laser powder bed fusion · Inconel 718 · Heat treatment

1 Introduction

Inconel 718 is a well-known nickel-based superalloy that features high strength at high temperatures, high yield strength, high fatigue properties, wear resistance, good

weldability, excellent creep properties, oxidation resistance and great corrosion resistance [1–3]. Owing to these properties of Inconel 718, it has large use areas such as turbine blades, combustion chambers, aircraft engines, steam generators, fasteners, instrumentation parts, liquid-fueled rockets, nuclear reactors, pumps and molds [3–6]. However, manufacturing products from Inconel 718 by conventional methods (such as the machining process) are challenging because of the high rate of tool-wearing, high cutting resistance and low ductility of superalloys. On the other hand, Inconel 718 alloys generally have complex geometry and thin-walled structures. Using additive manufacturing (AM) methods is reasonable to solve this situation. Laser powder bed fusion (LPBF) is the most widely used AM method and offers many advantages compared to conventional manufacturing methods. Such include high geometrical complexity, reduction of production steps, low material consumption, reduction of lead time and the near-net-shape component's

Technical Editor: Izabel Fernanda Machado.

✉ Nedim Sunay
nedimsunay@eskisehir.edu.tr

¹ Department of Airframe and Powerplant Maintenance, Eskisehir Technical University, Eskisehir, Turkey

² Department of Mechanical Engineering, Piri Reis University, Istanbul, Turkey

³ Department of Mechanical Engineering, Engineering Faculty, Bursa Uludag University, Bursa, Turkey

⁴ Department of Mechanical Engineering, Technology Faculty, Marmara University, Istanbul, Turkey

production with minimal posttreatment or post-machining [4, 7]. LPBF-fabricated components may also have disadvantages such as high tensile residual stresses, poor surface quality, high porosity ratios and low mechanical properties due to microstructure [8, 9].

The complexity of the LPBF process affects the microstructure of the LPBF-fabricated part and its physical and chemical behavior in the melt pool [10, 11]. Several process parameters can influence the fabrication process and must be carefully adjusted to produce parts without defects such as porosity, cracks and altered chemical composition by selective vaporization [12]. These process parameters can be related to scan (scan speed, hatch spacing, scan strategy), laser (laser power, spot size, pulse duration, pulse frequency) and powder (layer thickness, particle size, particle shape, powder bed density, material properties) [13]. Since the selected process parameters affect the energy density, the porosity ratio, the dimensions of the cellular and columnar grain structures formed in the microstructure of the materials vary according to the parameters used. Therefore, the size of the grains and the porosity ratio affect the hardness values of the materials. Accordingly, the mechanical properties of the parts are influenced differently by each LPBF process parameter [14–16]. Related to volumetric energy densities depend on applying laser power. These changes affect many properties, and one of them is the melt pool depth [17]. Another process parameter is spot size, which can modify via laser focus shift. Studies have shown that when the laser spot size increases, the surface roughness decreases, and the porosity in the internal structure decreases significantly [18]. And parameter related to powder, such as layer thickness, is one factor that directly affects surface roughness [19].

Although the poor surface aspect of printed metal components, including Inconel 718, is still discussed in AM community, process duration to fabricate components is also a significant factor affecting decision-makers to assess AM process's appropriateness as it directly affects the production

chain and the cost of the product. Therefore, this study examines the effect of scanning speed and laser power on material surface integrity, mechanical properties and the role of high hatch distance. It is well acknowledged that most studies in this area to fabricate components made of Inconel 718 powders prefer to use the hatch distance that is close to spot size or smaller [20–24]. Although this study proposes a reverse direction, in such cases, much energy density is needed so that more power is required. Changing the laser scanning speed is another way to adjust the volumetric energy density. This change also affects production time. Therefore, this study tried production with different speeds to serve both purposes. Thanks to the determination of the optimum process parameters, the surface, subsurface characteristics and mechanical properties of the Inconel 718 parts were relatively improved. However, these properties are insufficient because Inconel 718 components are used under high temperatures, dynamic loads and extreme conditions [25]. For this reason, post-processing operations, also studied in the literature, are indispensable [26]. Post-processing methods such as abrasive flow machining [27], ball burnishing [28], drag finishing [29], electropolishing [30], heat treatment [31], etc., are applied to the parts produced by additive manufacturing to enhance the material properties. Among these methods, heat treatment homogenizes the material's microstructure and reduces porosities and tensile residual stresses [32]. Although the heat treatment does not affect the surface quality, it changes the microstructure and therefore greatly affects the mechanical properties [33, 34]. Few studies in the literature investigate the effect of heat treatment on Inconel 718 parts produced with LPBF under various parameters [35]. However, there is no study examining the effect of heat treatment on Inconel 718 parts produced with LPBF under various laser power and scanning speed parameters, so more studies are needed in this particular area.

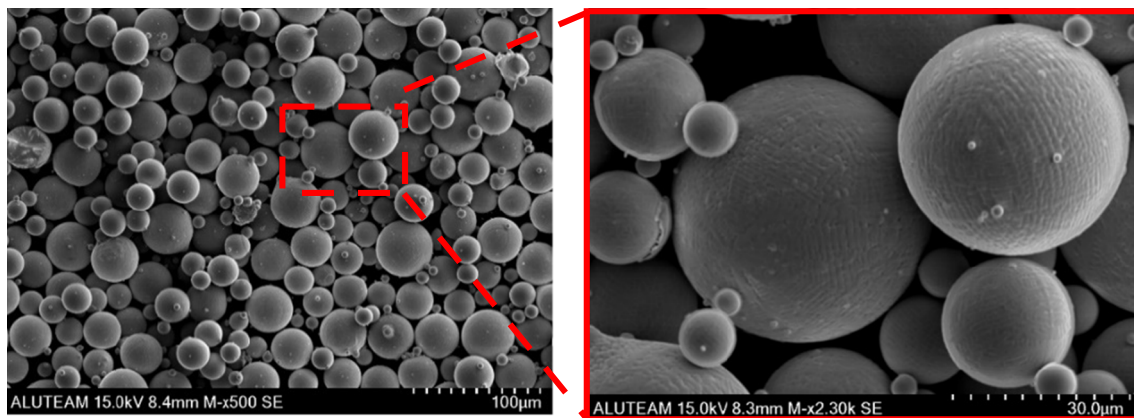


Fig. 1 SEM images showing Inconel 718 alloy powder morphology (500×, 2300×)

Table 1 Chemical composition (wt.%) of IN718 powder [36]

Ni	Cr	Nb + Ta	Mo	Ti	Al	Co	Cu	C	Si	Mn	Fe
50.0–55.0	17.0–21.0	4.75–5.50	2.80–3.30	0.65–1.15	0.20–0.80	0–1.00	0–0.30	0–0.08	0–0.35	0–0.35	Balance

2 Material and method

2.1 Powder material

Inert gas atomized pre-alloyed IN718 superalloy powders with the stated particle size of 15–45 μm was acquired from GE Additive's AP&C and used in this study. Figure 1 shows the morphology of the Inconel 718 alloyed powder particle images taken by a scanning electron microscope (SEM). Table 1 shows the chemical composition of powder provided by AP&C according to UNS N07718 in the case study brochure on GE Additive Machine X Line 2000R.

Table 2 Parameters of the LPBF process and volumetric energy densities of each parameter according to Equation 1

Constant parameters		
Hatch distance h , mm: 0.12		
Layer thickness d , mm: 0.03		
Laser focus diameter f_d , mm: 0.085		
Recoating time s , sec: 11		
Scan strategy: Stripe Rotate 90° Pattern		
Laser power P , (W)	Laser scan speed V , (mm/s)	The volumetric energy density (J/mm^3)
145	700	57.5
	1000	40.3
	1300	30.9
190	700	75.4
	1000	52.8
	1300	40.6
235	700	93.3
	1000	65.3
	1300	50.2
280	700	111.1
	1000	77.8
	1300	59.8
325	700	128.9
	1000	90.3
	1300	69.4
370	700	146.9
	1000	102.8
	1300	79.1

2.2 Manufacturing process

Samples are produced using the LPBF method from Inconel 718 superalloy material in the “EnaVision 3D Additive Manufacturing Machine” with the process parameters shown in Table 2. This machine has a type of laser with max. power of 500 W and a spot diameter of 85 μm . Parts of 15 mm \times 15 mm \times 15 mm size are arranged on the base plate as shown in Fig. 2a. The strip rotation model under nitrogen atmosphere was adopted during the production process as a combing strategy. In particular, the scanning direction was rotated 90° clockwise for the subsequent layer, as shown in Fig. 2b. Based on a series of preliminary experiments, the laser power (P) was preset at 145, 190, 235, 280, 325 and 370 W, and scan speeds (V) were set at 700, 1000 and 1300 mm/s, as shown in Table 2. The following equation gives the relationship between these parameters and energy density.

$$E_d = \frac{P}{v \cdot h \cdot d} [\text{J}/\text{mm}^3] \quad (1)$$

where E_d is the energy density or energy input in J/mm^3 , P is the laser power (W), v is the laser scan speed (mm/s), h is the hatch distance (mm) and d is the layer thickness of the powder bed (mm)[12]. These variables are shown schematically in Fig. 2c. This equation has been used to determine process parameters in many research [37–41]. However, other important parameters affect this energy density even though they are not included in the equation, such as building orientation, scanning strategy, gas flow direction, laser offset and laser diameter.

2.3 Heat treatment

After material characterization of the parts, heat treatment was conducted to compare their material properties after heat treatment. Heat treatment was carried out in accordance with the AMS 5663 standard [42]. As-built parts were heat-treated as follows: to begin with, the components were heated up to a temperature of 980 $^{\circ}\text{C}$ for 2 h, holding parts at 980 $^{\circ}\text{C}$ for 1 h followed by air cooling rate of 8 $^{\circ}\text{C}/\text{min}$ to room temperature, then parts were aged at 720 $^{\circ}\text{C}$ with the holding time of 8 h followed by furnace cooling rate of 55 $^{\circ}\text{C}/\text{h}$ to 620 $^{\circ}\text{C}$ holding for another 8 h before air cooling as shown in Fig. 3.

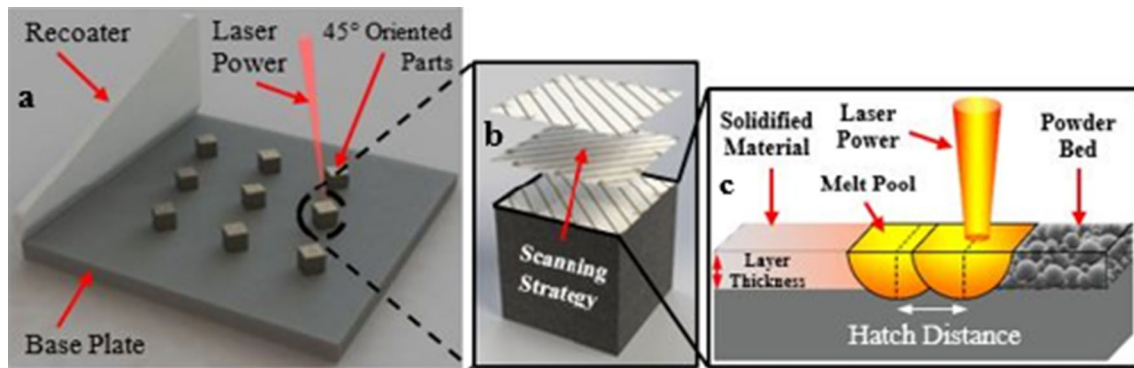


Fig. 2 a Arrangement of parts on the base plate, b scanning strategy and c PBF process main variables

2.4 Characterizations

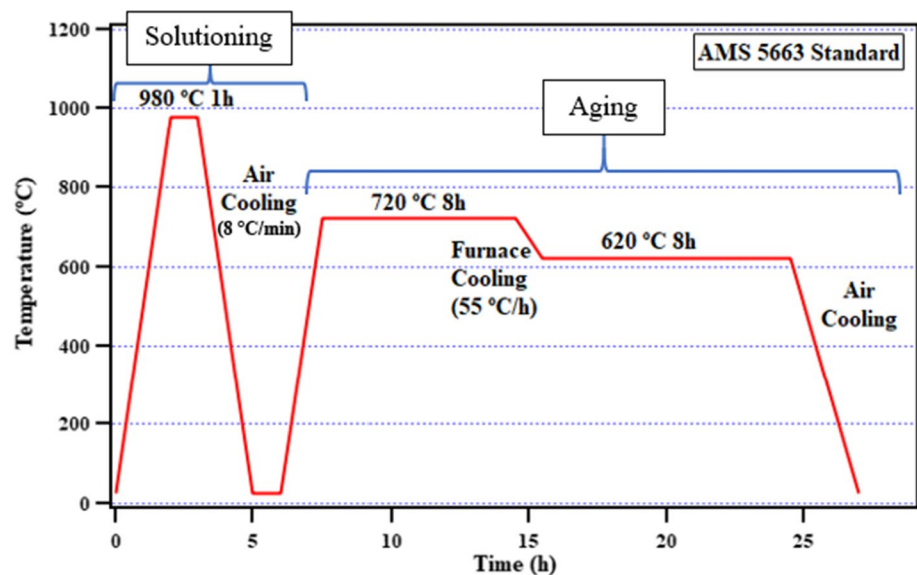
Specimens were cut with a diamond cutting disc, cold-mounting in acrylic and polishing using 60, 30 and 15 μm grit magnetic discs to examine the characterization. Specimens were etched using a solution of 15 ml HCl, 10 ml glycerol and 5 ml HNO_3 in fume cupboards to review the microstructure. All measurements were made at room temperature. A 3D Keyence VHX-6000 optical microscope was used to examine the microstructure and porosity. And microstructure was also characterized using a Philips XL30 field emission scanning electron microscopy (SEM) and X-ray diffraction (XRD) analysis. Brukers D8 (40 kW, 40 mA)-type X-ray diffractometer was used to identify the phases. XRD was operated with Cu $\text{K}\alpha$ radiation. Between 20° and 90° were scanned with an increment of 0.02° and account time of 1 s. Based on the data obtained from the XRD analysis, the formed phases are determined, and their effect on the mechanical

properties of the materials can be interpreted. Values obtained from XRD analysis are converted to graphs. Depending on the intensity and width of the resulting peaks, the changes in the part are interpreted.

2.5 Microhardness and wear test

The American Society for Testing and Materials (ASTM) E 384 standard was followed for the hardness test using Future-Tech FM310e. An average of 9 measurements determined the hardness of each specimen with a load dwelling time of 15 s, and a testing load of 100 gf was used. Dry sliding wear tests followed the ASTM G133 standard, using the TURKYUS RTW linear wear machine. Parts were tested for dry-sliding wear resistance before and after heat treatment at suitable room temperature, against 6-mm diameter tungsten carbide (tungsten carbide (WC) 94%, cobalt (Co) 6%) balls using a sliding

Fig. 3 The heat treatment process of additively manufactured Inconel 718



frequency of 2 Hz and a stroke length of 10 mm. The load was set at 5 N, and the total sliding distance was adjusted to 60 m.

3 Results and discussion

3.1 Porosity

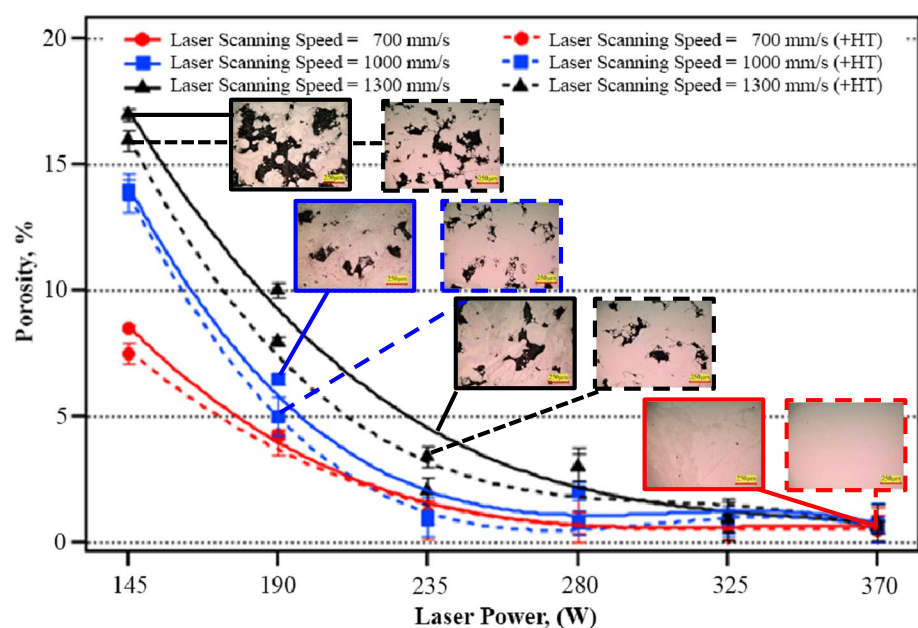
Porosity is one of the biggest problems in additive manufacturing and significantly affects parts' mechanical properties (yield strength, tensile strength, hardness, fatigue) [20, 43]. The porosity ratios of as-built and heat-treated parts are presented in Fig. 4. It is clearly seen that the porosity decreases with increasing laser power and decreasing laser scanning speed. This result shows agreement with the previous results [44]. In as-built parts, the highest porosity rate (17.3%) resulting from 145 W (laser power) to 1300 mm/s (scanning speed), while the lowest porosity rate (0.6%) resulting from 370 W (laser power) to 700 mm/s (scanning speed). Porosity may occur due to insufficient melting of the powder due to low energy density, or powder spatter and evaporation from over-melting due to high energy density [45]. Such defects reduce the effective load-bearing area perpendicular to the layers (building direction) and cause a notch effect, reducing static and dynamic strength in the building direction [46]. In the porosity rates after heat treatment, a decrease of 2.2% was determined for the parts fabricated with 145 W–1300 mm/s, while a decrease of 0.1% was determined for the parts fabricated with 370 W–700 mm/s. With the effect of high temperature during heat treatment, plastic deformation and then diffusion of atoms occur in the pores. This way,

the large pores are reduced in size, while the small pores are dissolved in the matrix [35]. In heat-treated parts, the highest porosity rate (15.1%) resulting from 145 W (laser power) to 1300 mm/s (scanning speed), while the lowest porosity rate (0.5%) resulting from 370 W (laser power) to 700 mm/s (scanning speed).

LPBF process was carried out in an inert gas (argon) atmosphere. The inert gas dissolved in the melting pool during production cannot leave the melting pool due to the high solidification rates, and the trapped gas bubbles produce metallurgical porosity in the parts [47]. According to previous studies, the high temperature caused by the increase in energy density causes low viscosity of the liquid and accelerates the movement and fluidity of the molten metal, so that the liquid metal flows and fills the pores easily [48, 49]. When the laser energy input is too low, large irregular pores are formed due to the high viscosity.

It is possible to say that the pores of the parts decrease after heat treatment. At low laser power and high laser scanning speed, the resulting porosity increases due to partially molten and entrapped powder particles that adhere to the outer edges of the solidified melt pool. This phenomenon is known as “satellite formation” or “hillocks” [50, 51]. These defects mainly occur when the powder particles are not given sufficient time or heat to penetrate the melting pool before solidification [52]. Another significant finding is the pores, which are very common in low-density parts, cause cracks starting from the edges of the coupon parts. Pore and crack formation are attributed to high tensile residual stresses in the literature [53]. A nearly nonporous structure was observed at high laser power, low laser scanning speed. Nevertheless, it should be noted that a few minor

Fig. 4 Porosity rates of as-built and heat-treated (+ HT) parts fabricated under different laser power and scanning speeds



imperfections are still visible. The pore seen as a very narrow crack may have occurred due to sample polishing and etching [54].

In this study, the hatch distance in the LPBF process was taken higher (120 μm) than the values in the literature. As the hatch distance increases, the distance between the melted powders will increase, so a full overlap could not be achieved; the energy density decreases and the lack of melting increases the porosity [55]. Since the hatch distance is higher than the laser focus diameter, the overlap of the melting regions in the surface layers is determined by the laser power and laser scanning speed, which are other parameters. However, in the studies in the literature, it has been reported that very high energy density causes the powder to spatter on the surface of each layer, and thus this situation closes the defects in the next layer and creates closed pores [56]. At the same time, the high energy density can create a keyhole with the recoil momentum produced by the evaporating metal [57]. In some studies, it has been stated that the effect of hatch distances on porosity can be minimized by optimizing the parameters of layer thickness, scanning strategy, laser power and laser scanning speed [58]. Thus, a homogeneous structure can be created at high scanning distances thanks to the large enough melting pools. On the other hand, the same study stated that low scanning distances lead to remelting, which did not significantly reduce the porosity level.

3.2 Microstructure

The microstructure of Inconel 718 parts produced by the LPBF process consists of cellular dendrites and columnar dendrites [2]. Figure 5 shows cellular dendritic structures and columnar grain structures. It is observed that the increase in the volumetric energy density due to the increase in laser power at the same laser scanning speed creates a more homogeneous melting pool structure up to a certain level, and then irregular melting pools are formed with the further increase in laser power. In addition, this increase in volumetric energy density results in more tightly connected cellular dendritic structures [59].

The hatch distance significantly affects the microstructure of the parts, as it plays an important role in the thermal

cycling of successive layers [60, 61]. Low hatch distance causes the melting pools to overlap, causing remelting of the previously solidified layer, resulting in high-temperature gradients. Due to these high temperatures, columnar grain structures in the microstructure are formed more densely and residual stress ratios increase [62]. Optimum laser power, scanning speed, layer thickness and scanning strategy should be chosen to minimize the disadvantage of the high hatch distance and make the melting pools and columns closer to each other and homogeneous [53].

The variation in the depths of the melting pools according to the laser power by keeping the laser scanning speed (1000 mm/s) constant and the variation according to the laser scanning speed by keeping the laser power (370 W) constant is presented in Fig. 6. It is clearly seen that the melt pool depth increased at higher laser power levels and decreased at higher scan speeds. As reported by previous researchers, this result shows that the depth of the melting pool varies depending on the energy density [5]. As the energy density increases, the depth of the melting pool increases. However, it should be noted that the continuous increase in the depth of the melt pool is not desirable, in regions where the laser beam's intensity is particularly high, the resulting melt pool can exhibit deep penetration and defects such as keyhole in the microstructure [59, 63]. Besides, at high scanning speeds, the depth of the melt pool becomes less due to the lower penetration of the laser power. In addition, high scanning rates can cause weak bonding and interlayer gaps. Therefore, defects such as keyholes form in the microstructure of the parts [59].

SEM images of the parts produced with different laser power and scanning speeds are presented in Fig. 7. In order to better understand the effects of both production parameters and energy densities on material properties, the part fabricated under 4 different parameter sets (145W–1300 mm/s = 30.9 J/mm³, 190W–700 mm/s = 75.4 J/mm³, 370W–1300 mm/s = 79.1 J/mm³, 370W–700 mm/s = 146.9 J/mm³) was selected. In the images, blue arrows indicate cellular dendritic structures, yellow arrows indicate columnar grain structures and red arrows indicate equiaxed grain structures. These structures

Fig. 5 Microstructure images of as-built parts fabricated under 1000 mm/s scanning speed and different laser powers (145–280–370 W)

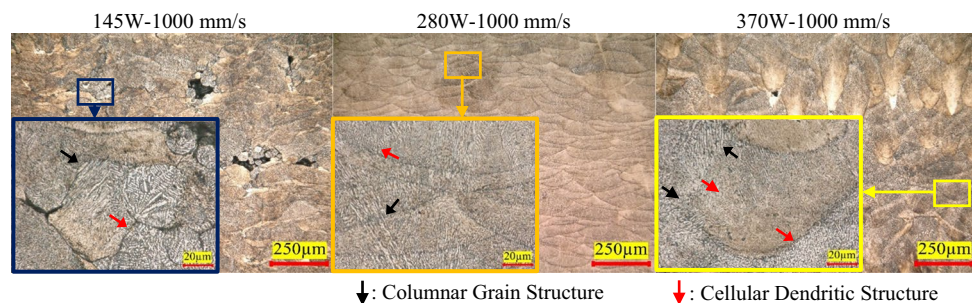
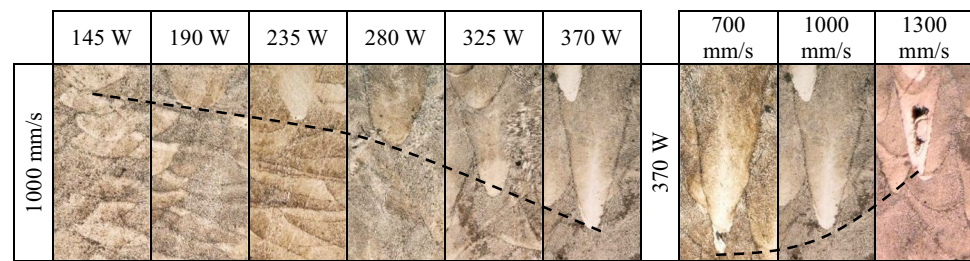


Fig. 6 Melting pool depths of the LPBF parts fabricated under different production parameters



are separated from each other by the grain boundaries indicated by the dashed line [64].

It is noted that the growth direction of the columnar structures varies in different regions, as indicated by the yellow arrows in the microstructure of the parts produced at 190 W, 370 W laser power and 700 mm/s speed. This indicates that the temperature field inside the melting pool is complex, even though the overall heat flow direction is approximately parallel to the built direction [65]. It is clearly seen that the formation of columnar structures becomes more prominent at low speeds. This is due to the longer contact time of the laser beam with the powder at low speeds. In addition, the direction of the columnar structures in part produced with 370 W–700 mm/s is more balanced, and this is because the melting is better, and the heat flow is more balanced with the increase in energy density [65]. The grains transformed into columnar grains along the built direction in regions with high laser energy input. In contrast, in regions with low energy input, the grains grew in equiaxed grain structures. Under higher energy input, a higher temperature gradient facilitated columnar grain growth [66]. As for regions with low energy input, the temperature gradient is smaller. The metals in the previous layer were not sufficiently remelted. This leads to the formation of equiaxed grains [67, 68]. Besides, it can be concluded that as the energy density increases, coarser cellular dendritic structures are formed [66].

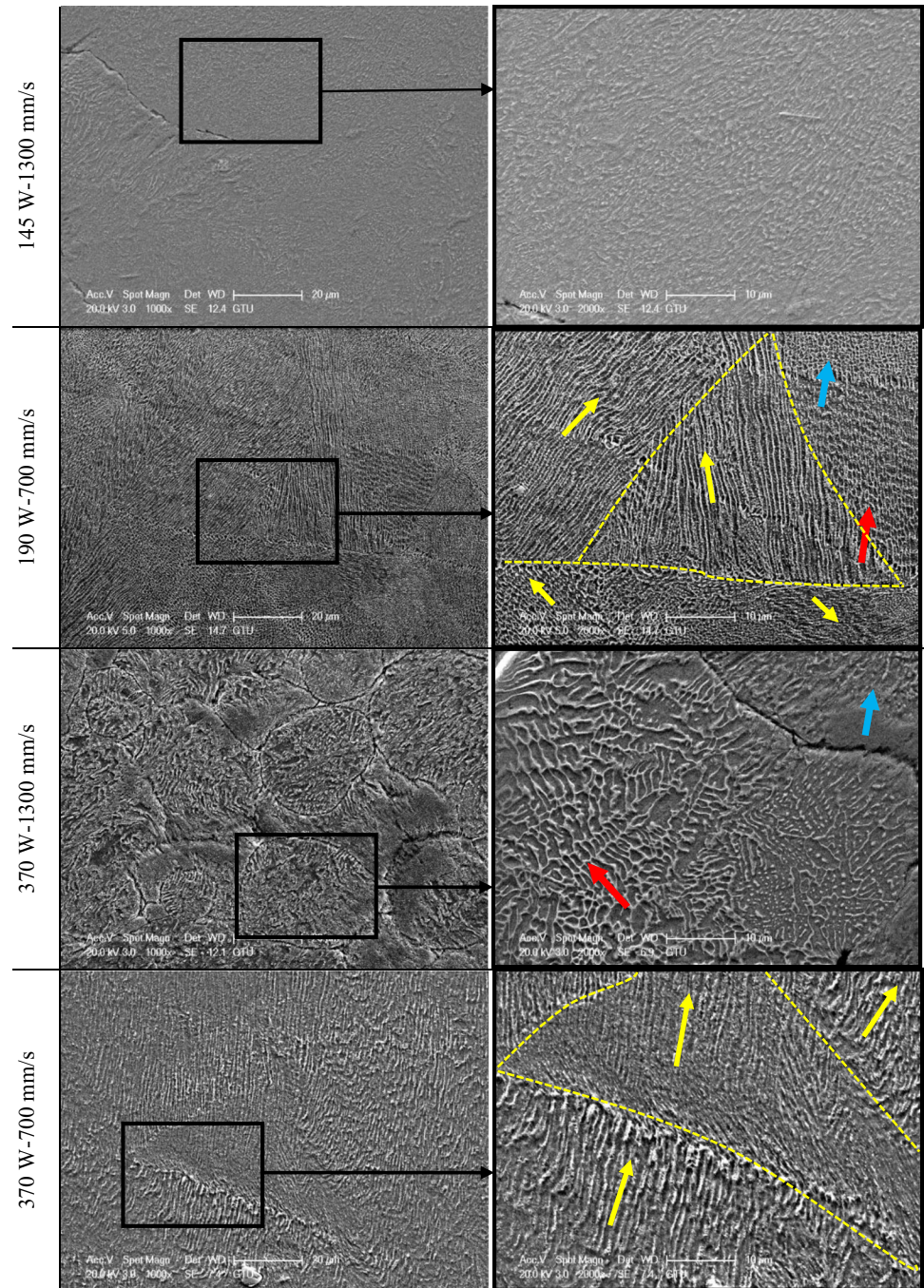
SEM images of the heat-treated parts fabricated under different laser power, and scanning speeds are presented in Fig. 8. Based on these results, the heat treatment significantly affects the microstructure of the parts. Melt pool boundaries, cellular dendritic structures and columnar grain structures in the as-built parts have completely disappeared, and grains and grain boundaries have formed instead. In the images, white arrows indicate Laves phase particles, yellow arrows indicate γ' , γ'' phases and red arrows indicate δ phase. In the SEM images of the heat-treated parts, Laves phase particles, indicated by white arrows, are seen as dispersed within the grain and along the grain boundaries. Laves phase is rich in Nb, Mo and Ti elements, while dendritic regions are rich in Ni, Fe and Cr elements [69]. During the heat treatment, the Laves phase dissolves, and the Nb element is released, forming the γ'' phase in the matrix. However,

in this study, large amounts of undissolved Laves particles were observed after the heat treatment, as seen in previous studies [70]. It is seen that these particles are more common in parts produced with low laser power (145 W) and high scanning speed (1300 mm/s) parameters. The fact that Laves phases are observed at the parameter 145W–1300 mm/s at the most, proves that the mechanical properties of the parts are lower than those produced with other parameters. When the scanning speed is kept constant at 1300 mm/s and the laser power is increased to 370W, it is observed that γ'' phases are formed due to the increase of γ' and Nb elements besides Laves particles [71]. It is seen that after the heat treatment of the piece produced with the parameter 190 W–700 mm/s, the needle-like δ phase is formed significantly, and the γ' phase is reduced. This indicates that the part's strength is lower than the part produced with 370 W–1300 mm/s. Because the conversion of the γ'' phase to the δ phase reduces the strength of the part [72]. After the heat treatment was applied to the part produced with 370 W–700 mm/s, it is possible to say that Laves and δ phases are not seen, but only γ' , γ'' phases. These phases greatly improve the material's mechanical properties by hindering the movement of dislocations [65, 73].

Figure 9 compares XRD patterns of as-built and heat-treated Inconel 718 parts fabricated under different parameters. According to the XRD analysis of the as-built parts, no phase was formed from the taenite (Fe, Ni) phase. Variations in peak intensities are related to the microhardness of the parts. Parts produced at different energy densities have the same phase distribution (γ and γ'' phases). XRD patterns have higher peak intensity in the (111) texture than in the (200) texture. Microstructures that can recrystallize and transform into γ'' phases caused an increase in peak intensities in the (200) texture. When the XRD results of the parts produced with 700 mm/s scanning speed and 190 W and 370 W laser powers are examined, it is seen that the peak intensity in the (200) texture is higher when the laser power is high. With increasing scanning speeds (from 700 to 1300 mm/s) at 370 W laser power, the peak intensity decreased in the (200) texture.

In XRD analysis of heat-treated parts, nickel–chromium oxide (NiCrO_3) phase was also found in addition to the taenite phase. Oxide structures occur in heat treatment

Fig. 7 SEM images of as-built Inconel 718 parts fabricated under different parameters (1000 \times , 2000 \times)



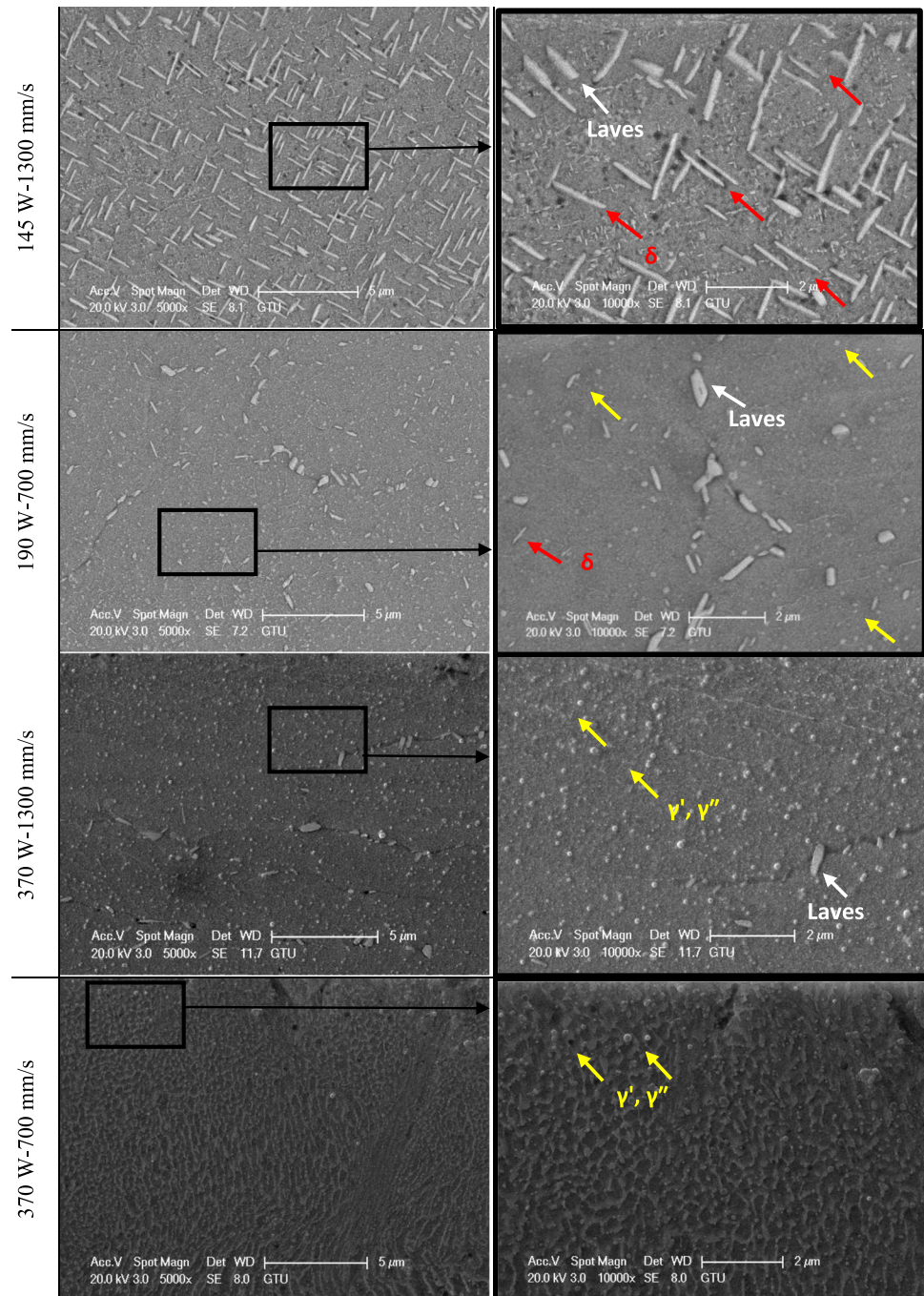
applications of parts at high temperatures as no inert gas is used during heat treatment [74]. When the XRD analysis of the heat-treated parts was examined, a differently δ (211) (Ni_3Nb) peak was formed [75, 76]. The formation of the δ -phase occurs after solution heat treatment [7]. The δ phase did not occur in as-built parts due to the high cooling rate and low Nb content [7]. It is known that the δ phase is present in the microstructure of as-built parts, but due to its small size, it could not be detected in XRD analyses before heat treatment [76]. In the parts after heat

treatment, it is seen that the peak intensities (111) texture increase and peak intensities (200) texture decrease with the effect of the solution heat treatment [77].

3.3 Microhardness and wear test

Microhardness variations of LPBF as-built and heat-treated Inconel 718 parts are presented in Fig. 10. As observed, with the increase in laser power and decrease in laser scanning speed, microhardness values of the parts

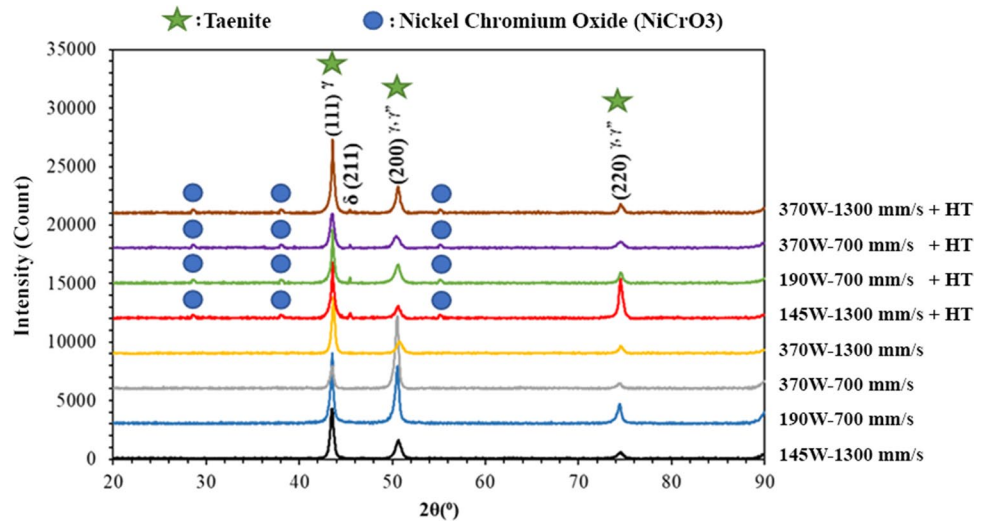
Fig. 8 SEM images of heat-treated Inconel 718 parts fabricated under different parameters (5000 \times , 10000 \times)



increase. Before heat treatment, the highest microhardness value (352.87 HV) was obtained under the conditions of 370 W laser power, 700 mm/s laser scanning speed and the lowest microhardness value (327.32 HV) was obtained under the conditions of 145 W laser power, 1300 mm/s laser scanning speed. After solution treatment and aging heat treatment, the microhardness value of each part increased by nearly 10%. This variation in hardness is attributed to the grain size reduction in the microstructure. This situation shows good agreement with the literature

[78]. It is obvious that although the main reason for these changes in microstructure is laser power, the scanning speed is an important factor as it affects the exposure time of the melting zone to laser power. Higher cooling rates cause larger residual stress in parts fabricated by LPBF, so the hardness of the parts can be reduced [79, 80]. It should also be noted that test points near the pores exhibited lower microhardness values than those tested in other regions [81, 82]. This proves that high energy inputs lead to relatively higher hardness.

Fig. 9 Comparison of XRD profiles of as-built and heat-treated (+ HT) LPBF-ed Inconel 718 samples



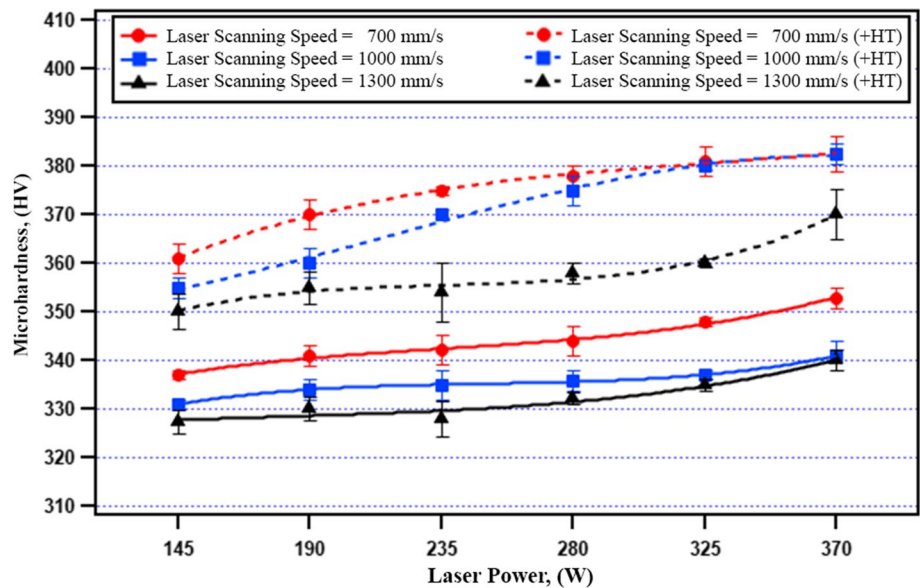
During production with LPBF, heat accumulates in the material due to repeated laser melting in the same area. Therefore, with the aging process, the γ' (body-centered tetragonal, BCT) precipitate phase begins to occur in the previously solidified layers. This phase, which has a BCT structure, increases the rigidity of the part.

Defects such as gas pores that occur under the surface of the parts during production due to insufficient melting times or laser powers significantly affect the microhardness values of the parts [83]. Obviously, with the increase of energy density, the porosity and defects decrease, the density of the parts is high and homogeneous under the surface, and this situation causes the microhardness values of the parts to be high [84]. Although grain refinement and precipitation in the microstructure of the parts according to the production parameters help to improve the

hardness of the parts produced with LPBF, heat treatment is required to improve the hardness [85]. The nano-sized γ' , γ'' phases and needle-shaped δ phase formed after heat treatment are the main reasons for the parts to reach high microhardness values. In addition, the high microhardness values are due to grain refinement and phase formation after heat treatment [85, 86].

Three-dimensional topography images of the wear traces taken by the optical microscope are presented in Fig. 11. In order to better compare the effect of production parameters and heat treatment on the wear performance of the parts, four different production parameter sets were selected. Among the as-built parts, it is seen that the maximum (48.43 μm) wear depth occurs in part produced with 145 W–1300 mm/s, and the lowest wear depth (36.65 μm) occurs in part produced with 370 W–700 mm/s. After the

Fig. 10 Microhardness values of as-built and heat-treated (+ HT) Inconel 718 fabricated under various laser power and scanning speed



heat treatment, a decrease of approximately 22% was determined for each parameter set in the wear depths.

Figure 12 shows the wear profiles of as-built and heat-treated Inconel 718 parts produced under different laser power and scanning speed. In the literature, the wear performance of materials is widely known to be associated with hardness. It is a well-known fact that increased hardness of material results in increased wear resistance of material [74]. The 7% increase in the hardness of the parts produced under different production parameters, and the 10% increase after heat treatment improved the

wear resistance of the parts. The part produced with the 370 W–700 mm/s parameter has the highest wear performance due to the minimum porosity and crack ratio [87]. Additionally, the γ' , γ'' phases formed in the microstructure of this part fix the grain boundaries and prevent boundary slippage [88]. This had a positive effect on the wear performance of the part. Residual stresses on the surface are lower in parts produced with the parameter 370 W–700 mm/s. High residual stress values cause crack formation in parts, which negatively affects wear performance. The reason for the significant improvement in

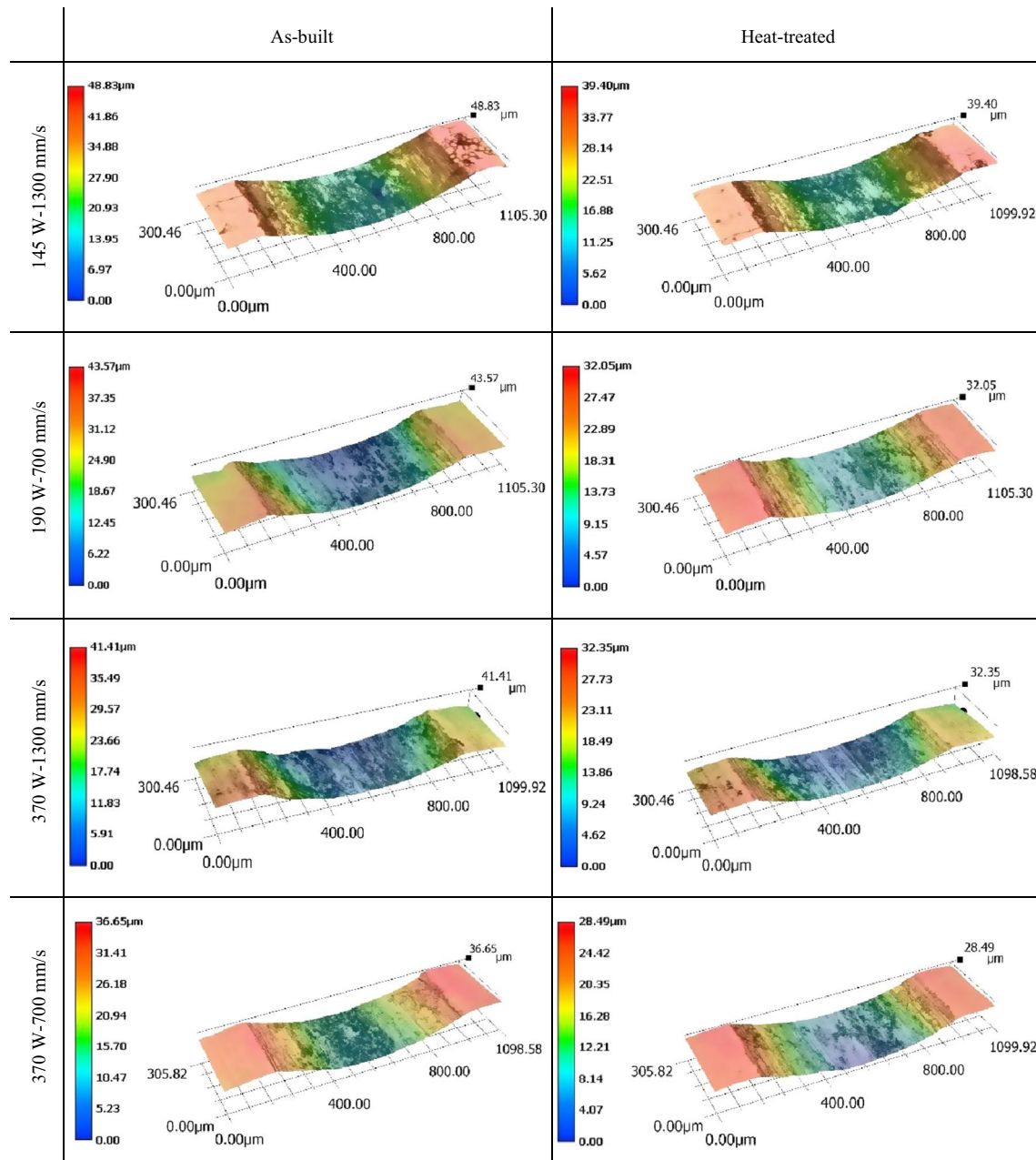


Fig. 11 3D wear topography images of LPBF as-built and heat-treated Inconel 718 parts

wear performance after heat treatment is the 96% reduction in residual stress values [89].

The wear volume was calculated using Eq. 2 defined below [90, 91]: where V , L , w and r are the wear volume (mm^3), the stroke length (mm), the width of the wear track (mm) and the radius of the carbide ball (mm), respectively.

$$V = L \left[r^2 \sin^{-1} \left(\frac{w}{2r} \right) - \frac{w}{2} \left(r^2 - \frac{w^2}{4} \right)^{\frac{1}{2}} \right] + \frac{\pi}{3} \left[2r^3 - 2r^2 \left(r^2 - \frac{w^2}{4} \right)^{\frac{1}{2}} - \frac{w^2}{4} \left(r^2 - \frac{w^2}{4} \right)^{\frac{1}{2}} \right] \tag{2}$$

The wear rate formula is given below:

$$k = \frac{V}{F \cdot s} \tag{3}$$

k (mm^3/Nm) is the specific wear rate, F (N) is the applied normal force and s (m) is the total sliding distance.

The specific wear rates of LPBF as-built and heat-treated Inconel 718 parts are presented in Fig. 13. Before heat treatment, the highest specific wear rate ($7984 \times 10^{-4} \text{ mm}^3/\text{Nm}$) was obtained under the conditions of 145 W laser power, 1300 mm/s laser scanning speed and the lowest specific wear rate ($6215 \times 10^{-4} \text{ mm}^3/\text{Nm}$) was obtained under the conditions of 370 W laser power, 700 mm/s laser scanning speed. After solution treatment and aging heat treatment, the specific wear rates of the parts decreased by 5–14%.

The highest wear resistance occurs in the parts produced with parameters with high energy density, and the lowest wear resistance occurs in parts with parameters

with low energy density. After the heat treatment application, it is clearly seen that the wear resistance increases at the same rate as the increase in the microhardness of each of the parts. After heat treatment, strengthening phases (γ' and γ'' phase) were formed, which reduced the shear force caused by sliding during the wear test and increased wear resistance, and an increase in wear resistance was observed in the parts [75, 92].

4 Conclusions

This study presents the effects of different laser power and laser scanning speeds and heat treatment on material properties of Inconel 718 parts fabricated under high hatch distance by the LPBF method. The results obtained as follows;

- Before heat treatment, the highest porosity rate of 17.3% was obtained in the part produced with the highest scanning speed and the lowest laser power (145 W–1300 mm/s), and the lowest porosity rate of 0.6% was obtained in the part produced with the lowest scanning speed and the highest laser power (370 W–700 mm/s). After the heat treatment, it was observed that the pore ratio of the parts decreased slightly. Heat treatment changes the parts' internal grain structure and microstructure, thus reducing their pores and increasing their density.
- According to the microstructure analysis, good stacking of the melting pools was observed in the regions with high energy input, while the irregularity of the melting pools between adjacent layers was observed under low energy input. It has been observed that the depth of the melt pool increases in direct proportion to the laser

Fig. 12 Wear profiles of as-built and heat-treated (+HT) Inconel 718 parts fabricated under different parameters

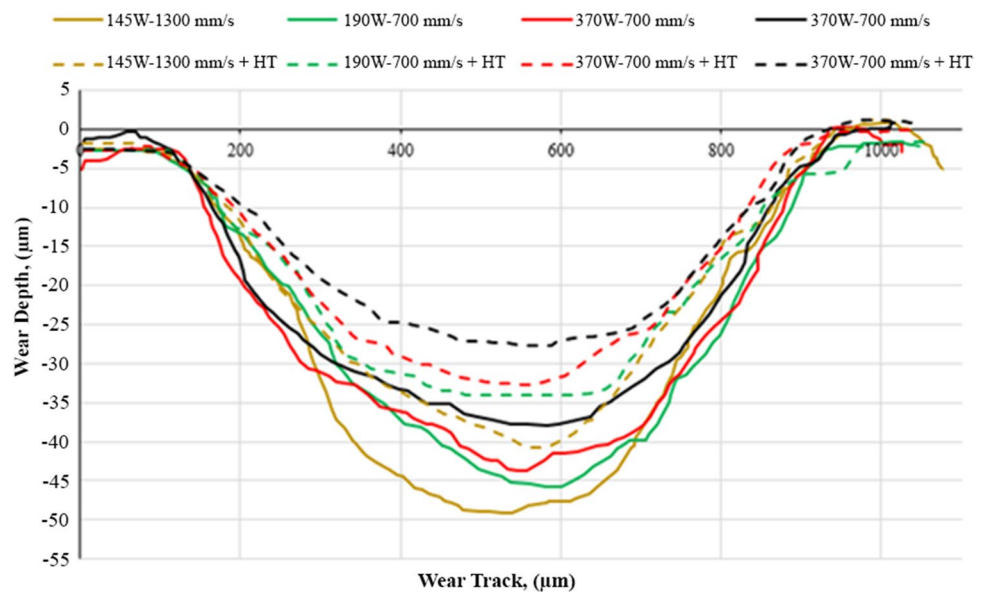
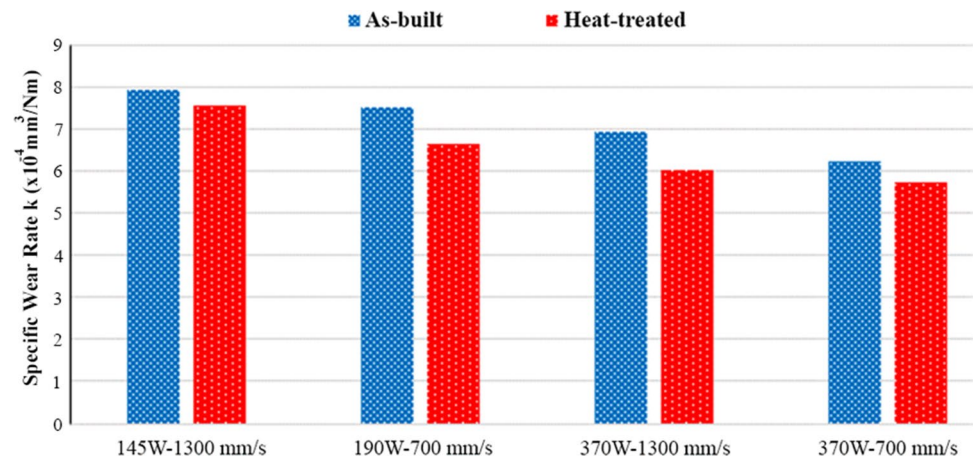


Fig. 13 The specific wear rates of as-built and heat-treated Inconel 718 were fabricated under various laser power and scanning speed



power when the scanning speed is constant, and the melt pool depth decreases when the laser power is kept constant and the scanning speed is increased. Additionally, the microstructure of Inconel 718 parts produced by the LPBF process consisted of cellular dendritic structures (cellular dendrites) and columnar grain structures (columnar dendrites). After the heat treatment, the melting pools completely disappeared and γ' , γ'' and δ phases were formed, as shown by SEM images.

- When the XRD results of the parts produced with 700 mm/s scanning speed and 190 W, 370W laser powers are examined, it is seen that the peak intensity in the (200) texture is higher when the laser power is high. With increasing scanning speeds (from 700 to 1300 mm/s) at 370 W laser power, the peak intensity decreased in the (200) texture. From these results, it was understood that the effect of laser scanning speed and laser power on recrystallization is inevitable. The formation of γ' , γ'' and δ phases after heat treatment was also supported by XRD analysis.
- It was concluded that the microhardness values of Inconel 718 parts increased with the energy density increase. After heat treatment, the microhardness value of each part increased by about 10%.
- Among the as-built parts, it has been determined that the highest wear resistance occurs in the parts produced with parameters with high energy density, and the lowest wear resistance occurs in parts produced with parameters with low energy density. After the heat treatment application, it was clearly seen that the wear resistance increased at the same rate as the increase in the microhardness of each of the parts. Considering the changes in microhardness and wear resistance, it has been understood how sensitive the mechanical properties are to microstructural changes.

Thanks to this study, it has been understood that by applying a high hatch distance and choosing optimum production parameters, parts close to the desired properties in the industry can be produced faster, and the mechanical properties

can be improved by the applied heat treatment, reducing the need for post-processing methods, thus it will be economically beneficial. Nevertheless, post-processing methods are inevitable for parts working under harsh conditions.

Declarations

Conflict of interest The authors declare no competing interests.

References

1. Popovich AA, Sufiarov VS, Polozov IA, Borisov EV (2015) Microstructure and mechanical properties of Inconel 718 produced by SLM and subsequent heat treatment. In: Key Engineering Materials. Trans Tech Publ. <https://doi.org/10.4028/www.scientific.net/KEM.651-653.665>
2. Jia Q, Gu D (2014) Selective laser melting additive manufacturing of Inconel 718 superalloy parts: densification microstructure and properties. *J Alloys Compd* 585:713–721. <https://doi.org/10.1016/j.jallcom.2013.09.171>
3. Lu Y, Wu S, Gan Y, Huang T, Yang C, Junjie L, Lin J (2015) Study on the microstructure mechanical property and residual stress of SLM Inconel-718 alloy manufactured by differing island scanning strategy. *Opt Laser Technol* 75:197–206. <https://doi.org/10.1016/j.optlastec.2015.07.009>
4. Nguyen QB, Nai MLS, Zhu Z, Sun C-N, Wei J, Zhou W (2017) Characteristics of inconel powders for powder-bed additive manufacturing. *Engineering* 3(5):695–700. <https://doi.org/10.1016/J.ENG.2017.05.012>
5. Kumar P, Farah J, Akram J, Teng C, Ginn J, Misra M (2019) Influence of laser processing parameters on porosity in Inconel 718 during additive manufacturing. *Int J Adv Manuf Technol* 103(1):1497–1507. <https://doi.org/10.1007/s00170-019-03655-9>
6. Kulawik K, Buffat P, Kruk A, Wusatowska-Sarnek A, Czyska-Filemonowicz A (2015) Imaging and characterization of γ' and γ'' nanoparticles in Inconel 718 by EDX elemental mapping and FIB–SEM tomography. *Mater Charact* 100:74–80. <https://doi.org/10.1016/j.matchar.2014.12.01>
7. Popovich V, Borisov E, Popovich A, Sufiarov VS, Masaylo D, Alzina L (2017) Impact of heat treatment on mechanical behaviour of Inconel 718 processed with tailored microstructure by selective laser melting. *Mater Des* 131:12–22. <https://doi.org/10.1016/j.matdes.2017.05.065>

8. Cai C, Zhou K (2022) Metal additive manufacturing. *Digit Manuf*. <https://doi.org/10.1016/B978-0-323-95062-6.00005-X>
9. Sanchez S, Smith P, Xu Z, Gaspard G, Hyde CJ, Wits WW, Ashcroft IA, Chen H, Clare A (2021) Powder bed fusion of nickel-based superalloys: a review. *Int J Mach Tools Manuf* 165:103729. <https://doi.org/10.1016/j.ijmactools.2021.103729>
10. Ho I-T, Chang K-C, Tiparti D, Yeh A-C, Tin S (2021) Insight to agglomeration and chemical reactions of CoAl_2O_4 inoculants in IN718 processed by selective laser melting. *J Alloys Compd* 883:160753. <https://doi.org/10.1016/j.jallcom.2021.160753>
11. Dursun G, Ibekwe S, Li G, Mensah P, Joshi G, Jerro D (2020) Influence of laser processing parameters on the surface characteristics of 316L stainless steel manufactured by selective laser melting. *Mater Today Proc* 26:387–393. <https://doi.org/10.1016/j.matpr.2019.12.061>
12. Prashanth K, Scudino S, Maity T, Das J, Eckert J (2017) Is the energy density a reliable parameter for materials synthesis by selective laser melting. *Mater Res Lett* 5(6):386–390. <https://doi.org/10.1080/21663831.2017.1299808>
13. Sing SL, Wiria FE, Yeong WY (2018) Selective laser melting of titanium alloy with 50 wt% tantalum: effect of laser process parameters on part quality. *Int J Refract Met Hard Mater* 77:120–127. <https://doi.org/10.1016/j.ijrmhm.2018.08.006>
14. Choi J-P, Shin G-H, Yang S, Yang D-Y, Lee J-S, Brochu M, Yu J-H (2017) Densification and microstructural investigation of Inconel 718 parts fabricated by selective laser melting. *Powder Technol* 310:60–66. <https://doi.org/10.1016/j.powtec.2017.01.030>
15. Greco S, Gutzeit K, Hotz H, Kirsch B, Aurich JC (2020) Selective laser melting (SLM) of AISI 316L—impact of laser power layer thickness and hatch spacing on roughness density and microhardness at constant input energy density. *Int J Adv Manuf Technol* 108(5):1551–1562. <https://doi.org/10.1007/s00170-020-05510-8>
16. Wan H, Zhou Z, Li C, Chen G, Zhang G (2019) Effect of scanning strategy on mechanical properties of selective laser melted Inconel 718. *Mater Sci Eng A* 753:42–48. <https://doi.org/10.1016/j.msea.2019.03.007>
17. Mirkoohi E, Sievers DE, Garmestani H, Chiang K, Liang SY (2019) Three-dimensional semi-elliptical modeling of melt pool geometry considering hatch spacing and time spacing in metal additive manufacturing. *J Manuf Processes* 45:532–543. <https://doi.org/10.1016/j.jmapro.2019.07.028>
18. Bean GE, Witkin DB, McLouth TD, Patel DN, Zaldivar RJ (2018) Effect of laser focus shift on surface quality and density of Inconel 718 parts produced via selective laser melting. *Addit Manuf* 22:207–215. <https://doi.org/10.1016/j.addma.2018.04.024>
19. Guan K, Wang Z, Gao M, Li X, Zeng X (2013) Effects of processing parameters on tensile properties of selective laser melted 304 stainless steel. *Mater Des* 50:581–586. <https://doi.org/10.1016/j.matdes.2013.03.056>
20. Koutiri I, Pessard E, Peyre P, Amlou O, De Terris T (2018) Influence of SLM process parameters on the surface finish porosity rate and fatigue behavior of as-built Inconel 625 parts. *J Mater Process Technol* 255:536–546. <https://doi.org/10.1016/j.jmatprotec.2017.12.043>
21. Chlebus E, Gruber K, Kuźnicka B, Kurzac J, Kurzynowski T (2015) Effect of heat treatment on the microstructure and mechanical properties of Inconel 718 processed by selective laser melting. *Mater Sci Eng A* 639:647–655. <https://doi.org/10.1016/j.msea.2015.05.035>
22. Kladovasilakis N, Charalampous P, Tsongas K, Kostavelis I, Tzovaras D, Tzetzis D (2022) Influence of selective laser melting additive manufacturing parameters in Inconel 718 superalloy. *Mater* 15(4):1362. <https://doi.org/10.3390/ma15041362>
23. Martínez S, Ortega N, Celentano D, Sánchez Egea AJ, Ukari E, Lamikiz A (2020) Analysis of the part distortions for Inconel 718 SLM: a case study on the NIST test artifact. *Mater* 13(22):5087. <https://doi.org/10.3390/ma13225087>
24. Anam MA, Pal D, Stucker B (2013) Modeling and experimental validation of nickel-based super alloy (Inconel 625) made using selective laser melting. In: International solid freeform fabrication symposium. Of Conference.: University of Texas at Austin. <http://dx.doi.org/https://doi.org/10.26153/tsw/15570>
25. Bourell D, Kruth JP, Leu M, Levy G, Rosen D, Beese AM, Clare A (2017) Materials for additive manufacturing. *CIRP Ann* 66(2):659–681. <https://doi.org/10.1016/j.cirp.2017.05.009>
26. Sunay N, Mert K, Kaynak Y (2020) Chemical post-processing methods for enhancing surface properties of parts fabricated by additive manufacturing: a review. *Sigma J Eng Nat Sci* 38(4):2027–2042
27. Atzeni E, Barletta M, Calignano F, Iuliano L, Rubino G, Tagliaferri VJAM (2016) Abrasive fluidized bed (AFB) finishing of AISi10Mg substrates manufactured by direct metal laser sintering (DMLS). *Addit Manuf* 10:15–23. <https://doi.org/10.1016/j.addma.2016.01.005>
28. Hiegemann L, Agarwal C, Weddeling C, Tekkaya AE (2016) Reducing the stair step effect of layer manufactured surfaces by ball burnishing. In: AIP Conference Proceedings AIP Publishing. <https://doi.org/10.1063/1.4963612>
29. Kaynak Y, Tascioglu E (2019) Post-processing effects on the surface characteristics of Inconel 718 alloy fabricated by selective laser melting additive manufacturing. *Progress Addit Manuf*. <https://doi.org/10.1007/s40964-019-00099-1>
30. Tyagi P, Goulet T, Riso C, Stephenson R, Chuenprateep N, Schlitzer J, Benton C, Garcia-Moreno F (2019) Reducing the roughness of internal surface of an additive manufacturing produced 316 steel component by chempolishing and electropolishing. *Addit Manuf* 25:32–38. <https://doi.org/10.1016/j.addma.2018.11.001>
31. Karabulut Y, Tascioglu E, Kaynak Y (2021) Heat treatment temperature-induced microstructure microhardness and wear resistance of Inconel 718 produced by selective laser melting additive manufacturing. *Optik* 227:163907. <https://doi.org/10.1016/j.ijleo.2019.163907>
32. Zhang D, Niu W, Cao X, Liu Z (2015) Effect of standard heat treatment on the microstructure and mechanical properties of selective laser melting manufactured Inconel 718 superalloy. *Mater Sci Eng A* 644:32–40. <https://doi.org/10.1016/j.msea.2015.06.021>
33. Jiang R, Mostafaei A, Wu Z, Choi A, Guan P-W, Chmielus M, Rollett AD (2020) Effect of heat treatment on microstructural evolution and hardness homogeneity in laser powder bed fusion of alloy 718. *Addit Manuf* 35:101282. <https://doi.org/10.1016/j.addma.2020.101282>
34. Fayed EM, Saadati M, Shahriari D, Brailovski V, Jahazi M, Medraj M (2021) Effect of homogenization and solution treatments time on the elevated-temperature mechanical behavior of Inconel 718 fabricated by laser powder bed fusion. *Sci Rep* 11(1):1–17. <https://doi.org/10.1038/s41598-021-81618-5>
35. Gruber K, Stopyra W, Kobiela K, Madejski B, Malicki M, Kurzynowski T (2022) Mechanical properties of Inconel 718 additively manufactured by laser powder bed fusion after industrial high-temperature heat treatment. *J Manuf Process* 73:642–659. <https://doi.org/10.1016/j.jmapro.2021.11.053>
36. Baicheng Z, Xiaohua L, Jiaming B, Junfeng G, Pan W, Chen-nan S, Muiling N, Guojun Q, Jun W (2017) Study of selective laser melting (SLM) Inconel 718 part surface improvement by electrochemical polishing. *Mater Des* 116:531–537. <https://doi.org/10.1016/j.matdes.2016.11.103>
37. Bertoli US, Wolfer AJ, Matthews MJ, Delplanque J-PR, Schoenung JM (2017) On the limitations of volumetric energy density

- as a design parameter for selective laser melting. *Mater Des* 113:331–340. <https://doi.org/10.1016/j.matdes.2016.10.037>
38. Carter LN, Wang X, Read N, Khan R, Aristizabal M, Essa K, Attallah MM (2016) Process optimisation of selective laser melting using energy density model for nickel based superalloys. *Mater Sci Technol* 32(7):657–661. <https://doi.org/10.1179/1743284715Y.0000000108>
39. Pal S, Gubeljak N, Hudak R, Lojen G, Rajtukova V, Predan J, Kokol V, Drstvensek I (2019) Tensile properties of selective laser melting products affected by building orientation and energy density. *Mater Sci Eng A* 743:637–647. <https://doi.org/10.1016/j.msea.2018.11.130>
40. Ghayoor M, Lee K, He Y, Chang C-H, Paul BK, Pasebani S (2020) Selective laser melting of 304L stainless steel: role of volumetric energy density on the microstructure texture and mechanical properties. *Addit Manuf* 32:101011. <https://doi.org/10.1016/j.addma.2019.101011>
41. Ciurana J, Hernandez L, Delgado J (2013) Energy density analysis on single tracks formed by selective laser melting with CoCrMo powder material. *Int J Adv Manuf Technol* 68(5–8):1103–1110. <https://doi.org/10.1007/s00170-013-4902-4>
42. Teixeira Ó, Silva FJ, Atzeni E (2021) Residual stresses and heat treatments of Inconel 718 parts manufactured via metal laser beam powder bed fusion: an overview. *Int J Adv Manuf Technol* 113(11):3139–3162. <https://doi.org/10.1007/s00170-021-06835-8>
43. Moussaoui K, Rubio W, Mousseigne M, Sultan T, Rezaei F (2018) Effects of selective laser melting additive manufacturing parameters of Inconel 718 on porosity microstructure and mechanical properties. *Mater Sci Eng A* 735:182–190. <https://doi.org/10.1016/j.msea.2018.08.037>
44. Salem H, Carter L, Attallah M, Salem H (2019) Influence of processing parameters on internal porosity and types of defects formed in Ti6Al4V lattice structure fabricated by selective laser melting. *Mater Sci Eng A* 767:138387. <https://doi.org/10.1016/j.msea.2019.138387>
45. Yusuf SM, Chen Y, Boardman R, Yang S, Gao N (2017) Investigation on porosity and microhardness of 316L stainless steel fabricated by selective laser melting. *Metals* 7(2):64. <https://doi.org/10.3390/met7020064>
46. Kelbassa I (2006) Qualifizieren des Laserstrahl-Auftragschweißens von BLISKs aus Nickel- und Titanbasislegierungen Aachen Techn Hochsch Diss
47. Parida RP, Senthilkumar V (2021) Experimental studies of defect generation in selective laser melted Inconel 718 alloy. *Mater Today: Proc* 39:1372–1377. <https://doi.org/10.1016/j.matpr.2020.04.698>
48. Shishkovsky I, Morozov Y, Smurov I (2009) Nanostructural self-organization under selective laser sintering of exothermic powder mixtures. *Appl Surf Sci* 255(10):5565–5568. <https://doi.org/10.1016/j.apsusc.2008.09.090>
49. Wang L-z, Wang S, Wu J-j (2017) Experimental investigation on densification behavior and surface roughness of AlSi10Mg powders produced by selective laser melting. *Opt Laser Technol* 96:88–96. <https://doi.org/10.1016/j.optlastec.2017.05.006>
50. Tolochko NK, Mozharov SE, Yadroitsev IA, Laoui T, Froyen L, Titov VI, Ignatiev MB (2004) Balling processes during selective laser treatment of powders. *Rapid Prototyp J*. <https://doi.org/10.1108/13552540410526953>
51. Van Elsen M (2007) Complexity of Selective Laser Melting: a new optimisation approach
52. Mumtaz K, Hopkinson N (2010) Selective laser melting of thin wall parts using pulse shaping. *J Mater Process Technol* 210(2):279–287. <https://doi.org/10.1016/j.jmatprotec.2009.09.011>
53. Fonseca EB, Gabriel AH, Araújo LC, Santos PL, Campo KN, Lopes ES (2020) Assessment of laser power and scan speed influence on microstructural features and consolidation of AISI H13 tool steel processed by additive manufacturing. *Addit Manuf* 34:101250. <https://doi.org/10.1016/j.addma.2020.101250>
54. Leuders S, Thöne M, Riemer A, Niendorf T, Tröster T, Richard HA, Maier HJ (2013) On the mechanical behaviour of titanium alloy TiAl6V4 manufactured by selective laser melting: fatigue resistance and crack growth performance. *Int J Fatigue* 48:300–307. <https://doi.org/10.1016/j.ijfatigue.2012.11.011>
55. Huang J, Li M, Wang J, Pei Z, McIntyre P, Ma C (2021) Selective laser melting of tungsten: effects of hatch distance and point distance on pore formation. *J Manuf Process* 61:296–302. <https://doi.org/10.1016/j.jmapro.2020.11.034>
56. Leung CLA, Marussi S, Towrie M, Atwood RC, Withers PJ, Lee PD (2019) The effect of powder oxidation on defect formation in laser additive manufacturing. *Acta Mater* 166:294–305. <https://doi.org/10.1016/j.actamat.2018.12.027>
57. King WE, Barth HD, Castillo VM, Gallegos GF, Gibbs JW, Hahn DE, Kamath C, Rubenchik AM (2014) Observation of keyhole-mode laser melting in laser powder-bed fusion additive manufacturing. *J Mater Process Technol* 214(12):2915–2925. <https://doi.org/10.1016/j.jmatprotec.2014.06.005>
58. Kasperovich G, Haubrich J, Gussone J, Requena G (2016) Correlation between porosity and processing parameters in TiAl6V4 produced by selective laser melting. *Mater Des* 105:160–170. <https://doi.org/10.1016/j.matdes.2016.05.070>
59. Balbaa M, Mekhail S, Elbestawi M, McIsaac J (2020) On selective laser melting of Inconel 718: densification surface roughness and residual stresses. *Mater Des* 193:108818. <https://doi.org/10.1016/j.matdes.2020.108818>
60. Arısoy YM, Criales LE, Özel T, Lane B, Moylan S, Donmez A (2017) Influence of scan strategy and process parameters on microstructure and its optimization in additively manufactured nickel alloy 625 via laser powder bed fusion. *Int J Adv Manuf Technol* 90(5):1393–1417. <https://doi.org/10.1007/s00170-016-9429-z>
61. Carter LN, Martin C, Withers PJ, Attallah MM (2014) The influence of the laser scan strategy on grain structure and cracking behaviour in SLM powder-bed fabricated nickel superalloy. *J Alloys Compd* 615:338–347. <https://doi.org/10.1016/j.jallcom.2014.06.172>
62. Nadammal N, Cabeza S, Mishurova T, Thiede T, Kromm A, Seyfert C, Farahbod L, Haberland C, Schneider JA, Portella PD (2017) Effect of hatch length on the development of microstructure texture and residual stresses in selective laser melted superalloy Inconel 718. *Mater Des* 134:139–150. <https://doi.org/10.1016/j.matdes.2017.08.049>
63. Kusuma C (2016) The effect of laser power and scan speed on melt pool characteristics of pure titanium and Ti-6Al-4V alloy for selective laser melting
64. Lippold JC, Kiser SD, DuPont JN (2011) *Welding metallurgy and weldability of nickel-base alloys*. John Wiley & Sons, Hoboken
65. Huang W, Yang J, Yang H, Jing G, Wang Z, Zeng X (2019) Heat treatment of Inconel 718 produced by selective laser melting: microstructure and mechanical properties. *Mater Sci Eng A* 750:98–107. <https://doi.org/10.1016/j.msea.2019.02.046>
66. Wang X, Kang J, Wang T, Wu P, Feng T, Zheng L (2019) Effect of layer-wise varying parameters on the microstructure and soundness of selective laser melted INCONEL 718 alloy. *Mater* 12(13):2165. <https://doi.org/10.3390/ma12132165>
67. Popovich V, Borisov E, Popovich A, Sufiarov VS, Masaylo D, Alzina L (2017) Functionally graded Inconel 718 processed by additive manufacturing: crystallographic texture anisotropy of microstructure and mechanical properties. *Mater Des* 114:441–449. <https://doi.org/10.1016/j.matdes.2016.10.075>

68. Liu X, Zhao C, Zhou X, Shen Z, Liu W (2019) Microstructure of selective laser melted AlSi10Mg alloy. *Mater Des* 168:107677. <https://doi.org/10.1016/j.matdes.2019.107677>
69. Zhou L, Mehta A, McWilliams B, Cho K, Sohn Y (2019) Microstructure precipitates and mechanical properties of powder bed fused Inconel 718 before and after heat treatment. *J Mater Process Technol* 35(6):1153–1164. <https://doi.org/10.1016/j.jmst.2018.12.006>
70. Komarasamy M, Shukla S, Williams S, Kandasamy K, Kelly S, Mishra RS (2019) Microstructure fatigue and impact toughness properties of additively manufactured nickel alloy 718. *Addit Manuf* 28:661–675. <https://doi.org/10.1016/j.addma.2019.06.009>
71. Anderson M, Thiélin A-L, Bridier F, Bocher P, Savoie J (2017) δ Phase precipitation in Inconel 718 and associated mechanical properties. *Mater Sci Eng A* 679:48–55. <https://doi.org/10.1016/j.msea.2016.09.114>
72. Özer S (2020) Effect of post-processing heat treatment on the mechanical properties of Inconel 718 fabricated by selective laser melting *Fen Bilimleri Enstitüsü*
73. Raghavan S, Zhang B, Wang P, Sun C-N, Nai MLS, Li T, Wei J (2017) Effect of different heat treatments on the microstructure and mechanical properties in selective laser melted INCONEL 718 alloy. *Mater Manuf Process* 32(14):1588–1595. <https://doi.org/10.1080/10426914.2016.1257805>
74. Tascioglu E, Karabulut Y, Kaynak Y (2020) Influence of heat treatment temperature on the microstructural mechanical and wear behavior of 316L stainless steel fabricated by laser powder bed additive manufacturing. *Int J Adv Manuf Technol* 107(5):1947–1956. <https://doi.org/10.1007/s00170-020-04972-0>
75. Wang W, Wang S, Zhang X, Chen F, Xu Y, Tian Y (2021) Process parameter optimization for selective laser melting of Inconel 718 superalloy and the effects of subsequent heat treatment on the microstructural evolution and mechanical properties. *J Manuf Process* 64:530–543. <https://doi.org/10.1016/j.jmapro.2021.02.004>
76. Teng Q, Li S, Wei Q, Shi Y (2021) Investigation on the influence of heat treatment on Inconel 718 fabricated by selective laser melting: microstructure and high temperature tensile property. *J Manuf Process* 61:35–45. <https://doi.org/10.1016/j.jmapro.2020.11.002>
77. Fayed EM, Saadati M, Shahriari D, Brailovski V, Jahazi M, Medraj M (2021) Optimization of the post-process heat treatment of Inconel 718 superalloy fabricated by laser powder bed fusion process. *Metals* 11(1):144. <https://doi.org/10.3390/met11010144>
78. Balbaa M, Elbestawi M, McIsaac J (2019) An experimental investigation of surface integrity in selective laser melting of Inconel 625. *Int J Adv Manuf Technol* 104(9):3511–3529. <https://doi.org/10.1007/s00170-019-03949-y>
79. Liu F, Lin X, Yang G, Song M, Chen J, Huang W (2011) Microstructure and residual stress of laser rapid formed Inconel 718 nickel-base superalloy. *Opt Laser Technol* 43(1):208–213. <https://doi.org/10.1016/j.optlastec.2010.06.015>
80. Kaya M, Sunay N, Kaynak Y (2021) Comparison of finite element and empirical model prediction of surface residual stress in Inconel 718 parts fabricated by laser powder bed fusion additive manufacturing. *J Addit Manuf Technol* 1(3):592–592
81. Cherry J, Davies H, Mehmood S, Lavery N, Brown S, Siens J (2015) Investigation into the effect of process parameters on microstructural and physical properties of 316L stainless steel parts by selective laser melting. *Int J Adv Manuf Technol* 76(5):869–879. <https://doi.org/10.1007/s00170-014-6297-2>
82. Xu Y, Gong Y, Li P, Yang Y, Qi Y (2020) The effect of laser power on the microstructure and wear performance of IN718 superalloy fabricated by laser additive manufacturing. *Int J Adv Manuf Technol* 108(7):2245–2254. <https://doi.org/10.1007/s00170-020-05172-6>
83. Zhao X, Chen J, Lin X, Huang W (2008) Study on microstructure and mechanical properties of laser rapid forming Inconel 718. *Mater Sci Eng A* 478(1–2):119–124. <https://doi.org/10.1016/j.msea.2007.05.079>
84. Brown D, Li C, Liu Z, Fang X, Guo Y (2018) Surface integrity of Inconel 718 by hybrid selective laser melting and milling. *Virtual Phys Prototyp* 13(1):26–31. <https://doi.org/10.1080/17452759.2017.1392681>
85. Wang Z, Guan K, Gao M, Li X, Chen X, Zeng X (2012) The microstructure and mechanical properties of deposited-IN718 by selective laser melting. *J Alloys Compd* 513:518–523. <https://doi.org/10.1016/j.jallcom.2011.10.107>
86. Vilaro T, Colin C, Bartout J-D, Nazé L, Sennour M (2012) Microstructural and mechanical approaches of the selective laser melting process applied to a nickel-base superalloy. *Mater Sci Eng A* 534:446–451. <https://doi.org/10.1016/j.msea.2011.11.092>
87. Yu Z, Xu Z, Guo Y, Sha P, Liu R, Xin R, Li L, Chen L, Wang X, Zhang Z (2022) Analysis of microstructure mechanical properties wear characteristics and corrosion behavior of SLM-NiTi under different process parameters. *J Manuf Process* 75:637–650. <https://doi.org/10.1016/j.jmapro.2022.01.010>
88. Zhao Z, Li J, Bai P, Qu H, Liang M, Liao H, Wu L, Huo P, Liu H, Zhang J (2019) Microstructure and mechanical properties of TiC-reinforced 316L stainless steel composites fabricated using selective laser melting. *Metals* 9(2):267. <https://doi.org/10.3390/met9020267>
89. Wang T, Wang C, Li J, Chai L, Hu X, Ma Y, Huang Y (2021) Microstructure and wear properties of laser-clad NiCo alloy coating on Inconel 718 alloy. *J Alloys Compd*. <https://doi.org/10.1016/j.jallcom.2021.160412>
90. Sharma S, Sangal S, Mondal K (2013) On the optical microscopic method for the determination of ball-on-flat surface linearly reciprocating sliding wear volume. *Wear* 300(1–2):82–89. <https://doi.org/10.1016/j.wear.2013.01.107>
91. Yaman N, Sunay N, Kaya M, Kaynak Y (2022) Enhancing surface integrity of additively manufactured Inconel 718 by roller burnishing process. *Procedia CIRP* 108:681–686. <https://doi.org/10.1016/j.procir.2022.03.106>
92. Zhao Z, Qu H, Bai P, Li J, Wu L, Huo P (2018) Friction and wear behaviour of Inconel 718 alloy fabricated by selective laser melting after heat treatments. *Philos Mag Lett* 98(12):547–555. <https://doi.org/10.1080/09500839.2019.1597991>

Publisher's Note Springer Nature remains neutral with regard to jurisdictional claims in published maps and institutional affiliations.

Springer Nature or its licensor (e.g. a society or other partner) holds exclusive rights to this article under a publishing agreement with the author(s) or other rightsholder(s); author self-archiving of the accepted manuscript version of this article is solely governed by the terms of such publishing agreement and applicable law.